Ultrathin Paper Microsupercapacitors for Electronic Skin Applications

Mehmet Girayhan Say,* Ihor Sahalianov, Robert Brooke, Ludovico Migliaccio, Eric D. Głowacki, Magnus Berggren, Mary J. Donahue, and Isak Engquist

Ultrathin devices are rapidly developing for skin-compatible medical applications and wearable electronics. Powering skin-interfaced electronics requires thin and lightweight energy storage devices, where solution-processing enables scalable fabrication. To attain such devices, a sequential deposition is employed to achieve all spray-coated symmetric microsupercapacitors (μSCs) on ultrathin parylene C substrates, where both electrode and gel electrolyte are based on the cheap and abundant biopolymer, cellulose. The optimized spraying procedure allows an overall device thickness of ≈11 μm to be obtained with a 40% active material volume fraction and a resulting volumetric capacitance of 7 F cm^{-3}. Long-term operation capability (90% of capacitance retention after 10^4 cycles) and mechanical robustness are achieved (1000 cycles, capacitance retention of 98%) under extreme bending (rolling) conditions. Finite element analysis is utilized to simulate stresses and strains in real-sized μSCs under different bending conditions. Moreover, an organic electrochromic display is printed and powered with two serially connected μ-SCs as an example of a wearable, skin-integrated, fully organic electronic application.

1. Introduction

The growth of unconventional microelectronic devices in the fields of wearables, electronic skin, digitalization of health, transient, and implantable electronics has increased the demand for high-performance energy storage modules.[1–4] Among these, body-integrated, skin-inspired devices are receiving attention to achieve self-sustained batteries and supercapacitors that are extremely flexible and conform easily onto skin or biosurfaces.[5–8] As a first candidate, batteries manufactured on flexible substrates with vacuum deposition methods have recently been developed; however, the use of expensive cathodic materials, physical vapor deposition-based electrolytes, and area-limited fabrication make the device structure bulky and overcomplicated.[9–11] Thick substrates cause limited flexibility (high bending radius), reduced long-term cyclability, and high process expenses, which contradict the requirements of the skin-compatible electronics.[6] Due to these drawbacks, low-cost and large-area, high yield printed microsupercapacitors (μSCs) are intensely demanded. This has resulted in thin, planar devices, supplying high power density (quick charge delivery, in seconds) and cycling capability (more than 10 000 cycles) with the advantage of easy fabrication and scalable, straightforward solution-processing methods.[12,13] Printed μSCs from various carbon allotropes, conductive polymers, and Mxenes were fabricated as electrodes using different printing methods.[13–16] Thin substrates such as polyimide,[17] parylene C,[18] or PET foil with a carrier support[19] were employed for ultrathin electrochemical energy storage devices.

Conductive polymers are often considered inferior as a result of moderate energy delivery, their chemical stability, and the limited cyclability when compared to inorganic analogues. However, the possibility of low-cost printing onto a flexible substrate or polymerization into a scaffold allows the fabrication of porous electrodes with good capacitance cycling retention.[20,21]

M. G. Say, I. Sahalianov, E. D. Głowacki, M. Berggren,
M. J. Donahue, I. Engquist
Laboratory of Organic Electronics
Department of Science and Technology
Linköping University
Norrköping SE-601 74, Sweden
E-mail: mehmet.girayhan.say@liu.se

The ORCID identification number(s) for the author(s) of this article can be found under https://doi.org/10.1002/admt.202101420.

I. Sahalianov, L. Migliaccio, E. D. Głowacki
Bioelectronics Materials and Devices Laboratory
Brno University of Technology
Purkynova 123, Brno 61200, Czech Republic
R. Brooke
RISE Research Institutes of Sweden, Digital Systems
Smart Hardware
Bio- and Organic Electronics
Bredgatan 33, Norrköping SE-602 21, Sweden
M. Berggren, I. Engquist
Wallenberg Wood Science Center
Linköping University
Norrköping SE-601 74, Sweden

**ADVANCED
SCIENCE NEWS**
www.advancedsciencenews.com

**ADVANCED
MATERIALS
TECHNOLOGIES**
www.advmattechnol.de

One of the most studied conductive polymers, PEDOT (Poly(3,4-ethylenedioxythiophene)), exhibits efficient charge transport, low impedance, and high stability as a cathodic material.[22–25] The focus over the last decade has been dedicated to utilizing PEDOT-based materials, deposited through both electro-polymerization and vapor-phase (VP) methods or solution processed based methods, for the fabrication of microsupercapacitors.[21,23,26–28] Although electro- or VP-polymerization methods deliver high capacitance PEDOT, the fabrication process lacks thickness and area control, and therefore scalability.[21,26] Printing of water-dispersible PEDOT:PSS (PEDOT: polystyrene sulfonate) can overcome these limitations and provide control over the thickness, and extended area coverage, while maintaining sufficient energy density and environmentally friendliness without requirements of photolithography, surface treatment, or expensive infrastructure.[25,29,30]

The uniform film formation and functional ultrathin coating capability of spray coating through area control make it an excellent method to move from lab-scale devices to an industrial prototype level.[31,32] In the field of electrochemical device technology, spray coating has mostly involved fabrication of electrodes on thick substrates with nanometer-scale coating, which is not preferable for high energy density devices with desirable mechanics.[33,34] This can be overcome by using printed/sprayable inks with a cellulosic binder (nanofibrils, pulp, and particles) to provide porous, mechanically robust electrodes.[29,35] Moreover, spray coating of the gel electrolyte ensures control of the thickness and roughness of the gel surface, a tremendous advantage of spray coating compared to the widely used drop-casting method.[12,36] Therefore, printing/coating methods are promising candidates for maintaining the whole-cell thickness around 10 μm, which is necessary for skin-compatible electronics.[5,36]

Here, we demonstrate a paper-based micro-supercapacitor (P-μSC) fabricated by sequential coating/printing to achieve skin-compatible, flexible energy modules. Current collectors, paper electrodes (PEDOT: PSS/Cellulose Nanofibrils (CNF)), and cellulosic gel electrolytes were all deposited with shadow mask processes onto ultrathin parylene C substrates (2.8 μm). This fabrication approach does not require lithography processes, surface cleaning or activation, or high baking temperatures. Paper electrode ink and cellulose-based gel electrolyte ink formulations are spray coated with a simple airbrush onto interdigitated current collectors to achieve a compact device with a total thickness of 10.5 ± 0.3 μm and lateral dimensions of 1.8 × 2.4 cm^2. The thin P-μSC achieves up to 6.8 mF cm^{-2} areal and 7.0 F cm^{-3} volumetric capacitance and intermediate energy and power density (0.26 mWh cm^{-3} and 270 mW cm^{-3}). Outstanding charge–discharge cycle performance was demonstrated (capacitance retention of 90% after 10^4 cycles). Fabricated devices were proven to be mechanically stable and maintain full charge storage capability after 1000 bending cycles with a retained initial capacitance of 98% (bending radius of 6 mm). Detailed finite element method (FEM) simulations were carried out to analyze the mechanical properties of a device with different thickness of its parts at bending radius down to 6 mm. In particular, the simulations demonstrate maximum volumetric strain of 0.007% in the substrate, and 0.045% in electrode domain. Furthermore, an on-chip energy storage module was designed by connecting two μSCs in series to power a printed electrochromic display, demonstrating great potential for powering skin-interfaced and wearable electronics.
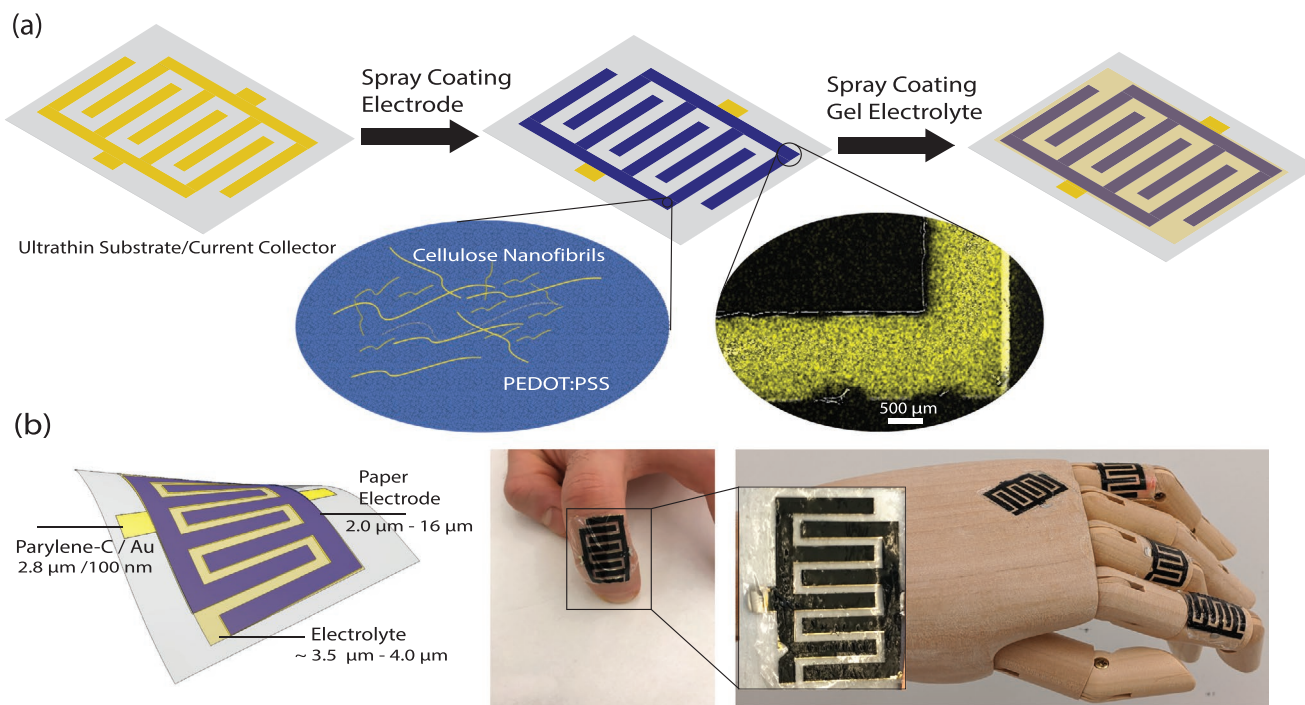

(a)

Spray Coating Electrode

Spray Coating Gel Electrolyte

Ultrathin Substrate/Current Collector

Cellulose Nanofibrils

PEDOT:PSS

500 μm

(b)

Paper Electrode
2.0 μm – 16 μm

Parylene-C / Au
2.8 μm /100 nm

Electrolyte
~ 3.5 μm – 4.0 μm

Figure 1. a) Schematic of the fabrication process for spray coated, thin, paper microsupercapacitors. Inset (left): illustration of the paper electrode composed of CNF and PEDOT: PSS, inset (right): An SEM image shows the width of a finger electrode. b) Schematic and corresponding optical images of the devices on various substrates.

2. Results and Discussions

All spray-coated paper supercapacitors, comprising two four-finger electrodes, were fabricated by a few sequential deposition steps. **Figure 1**a shows the overall fabrication method for the μSC. Details of the fabrication and ink formulation are given in the Experimental Section. Briefly, an ultrathin parylene C (2.8 μm) was deposited on a glass carrier substrate. Cr/Au (5/95 nm) current collectors were deposited through a shadow mask to define the finger electrodes. Paper electrode ink was spray-coated onto patterned finger metal electrodes with different spray cycles to achieve various thicknesses of paper electrodes. Finally, a gel electrolyte (3.5–4.0 μm) was spray-coated onto the paper micro-electrodes. Following gelation of the electrolyte, the spray coated μSC was completed and the devices could be peeled from the carrier substrate. Figure 1b shows the skin-attachable, wearable μSCs after peeling off the devices.

Construction of ultrathin μSCs requires sequential spray coating of the paper electrode and cellulose-based gel electrolyte onto the parylene C/Cr/Au substrate. Controlling the thickness in solution-processed devices leads to optimized active material mass loading, component thickness, and overall package form. Since delamination and partial detachment of the electrode layer can significantly affect the charge storage, we investigate the impact of electrode thickness (active material loading) on electrochemical performance. During a typical experiment, paper electrodes are deposited onto the substrates, which were placed on a hot plate at 90 °C and the paper ink was sprayed through a stainless-steel shadow mask. The amount of sprayed ink defines the thickness of the paper electrodes (Figures S1 and S2, Supporting Information). The device geometry was kept constant for all the devices. The width $w = 2$ mm, distance between two finger electrodes $d = 1$ mm, and length of the electrode $l = 10$ mm, were chosen for this device structure design (Figure S3, Supporting Information). The minimum distance between the interdigitated electrodes ($w = 1$ mm) was selected to ensure the stability of the shadow mask fabrication (features lower than 1 mm may result in stainless steel mask failure). It should be noted that smaller device dimensions can be achieved by photolithography processes or laser scribing.[37] However, in this work, we fabricate μSCs using low cost, consecutive spray coating method through shadow masks directly onto the ultrathin substrates without surface treatment, i.e., plasma cleaning, silanization, etc. Many reports on supercapacitor fabrication use drop-casting of bulky gel electrolytes, which diminishes the control of the overall device thickness. We have achieved good flexibility and complete control of the defined area and volume by developing a gel electrolyte ink that can be deposited using spray coating. Overall, the fabrication protocol gives solution-processed, conformable μSCs capable of distributing power to e-skin applications with superior control on the overall thickness of the device (≈11 μm).

The μSCs were fabricated in a planar device architecture with different electrode thicknesses. Electrochemical characterization was conducted in a two-electrode configuration. The thickness-dependent electrochemical characterization of P-μSCs is given in **Figure 2**. Figure 2a displays the cyclic voltammetry (CV) at 20 mV s^{-1} of P-μSCs, which have various
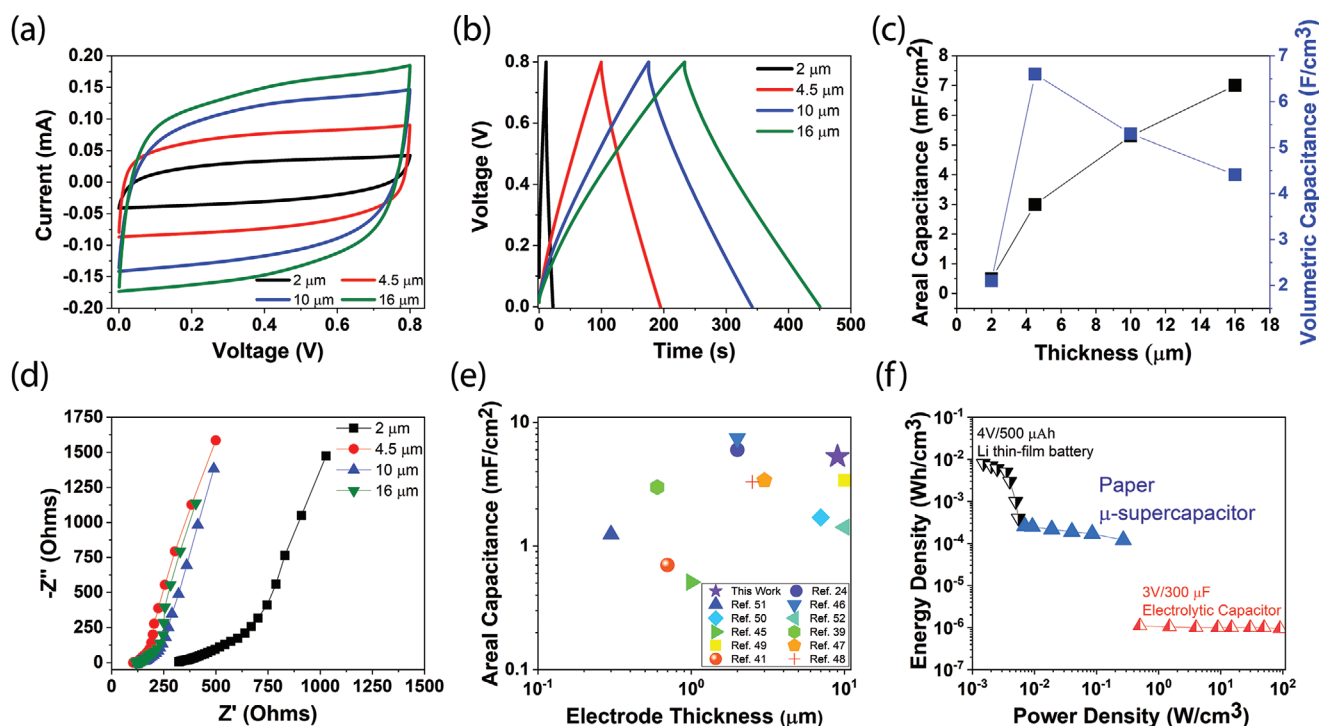

Figure 2. Thickness dependent electrochemical characterization of printed micro-supercapacitors. a) CV of paper supercapacitors at scan rate 20 mV s^{-1}. b) GCD at a current density of 0.025 mA cm^{-2}. c) Areal and volumetric capacitances of the microsupercapacitors depending on electrode thickness. d) Impedance spectroscopy of the microsupercapacitors with different electrode thickness. e) Comparison of electrode thickness versus areal capacitance. f) Ragone plot for comparison of paper microsupercapacitor with the available commercial devices (Li thin film battery[52] and Al electrolytic capacitor[55]).

paper electrode thicknesses. The devices show quasirectangular voltammograms, indicating that they exhibit a small resistive component. It can be seen from the CV curves that thicker electrodes with more active material demonstrate higher currents. To evaluate the capacitance and voltage (IR) drop, a galvanostatic charge discharge (GCD) test was performed at a current level of 0.025 mA cm^{-2}. Symmetric, triangular charge-discharge curves were recorded (Figure 2b). The devices show IR drops of 120, 20, 24, 23 mV at 0.025 mA cm^{-2} for paper electrodes of 2, 4.5, 10, 16 µm thick, respectively. The calculated areal and volumetric capacitances at a current density of 0.025 mA cm^{-2} are given in Figure 2c for the devices with different paper electrode thicknesses. The areal capacitance of the devices increased proportionally with electrode thickness due to the higher material loading for the defined 2.4 cm^2 area. The maximum areal capacitance of 6.8 mF cm^{-2} was reached for the 16 µm thick paper electrode. However, the highest volumetric capacitance (7.0 F cm^{-3}) was found for the device, which has 4.5 µm paper electrode thickness ($\approx$ 10.5 $\pm$ 0.3 µm, overall thickness). This behavior can be explained by a phenomenon that in the case of thicker films, ion penetration may be diminished due to the thickness, limiting charge transport. This has been observed in other materials that have volumetric capacitance property such as conductive polymers, Mxene, and composites.[38–40]

To investigate the equivalent series resistance (ESR) of µSCs with different paper electrode thicknesses, electrochemical impedance spectroscopy (EIS) was conducted from 100 kHz to 20 mHz, as shown in Figure 2d. The intercept of the x-axis (Z') at the Nyquist plot gives the ESR value at high frequencies. The device with a 4.5 µm paper electrode exhibits a quite low ESR of 103 Ω, and for the 10 and 16 µm paper electrodes show 116 and 125 Ω, respectively. ESR increases up to 320 Ω for the 2 µm electrode due to the low conductivity of the film (50 S cm^{-1}). The optimum performance was achieved for the 4.5 µm paper electrode, and the ESR value (103 Ω or 42.9 Ω cm^{-2}) is comparable or better than the previously published work, for example, PEDOT: PSS/MoO$_3$ (832.2 Ω)[41], reduced graphene oxide[42] (174 Ω), and graphene[43] (200 Ω cm^{-2}) based µSCs. Whereas the limiting factor for the shadow mask processes is the minimum dimension (for our case 1 mm) in between the interdigitated electrodes, reducing this dimension leads to lower ESR and higher areal/volumetric capacitance with the planar device structure.[37] Despite this patterning limitation, our devices perform better than the previous works using photolithography to create supercapacitors with performance of 5.23 F cm^{-3} and 100 Ω (interspace of 150 µm),[44] 2.4 mF cm^{-2} and $\approx$120 Ω (interspace of 50 µm)[45] and 3.47 mF cm^{-2} with 74.7 Ω (interspace of 50 µm).[46]

To evaluate the spray-coated electrode fabrication with other methods, a graph is given in Figure 2e for comparison of the obtained areal capacitance versus the electrode thickness (<10 µm). Our spray-coated paper electrodes outperform other spray-deposited devices such as graphene, carbon nanotubes, and PEDOT in terms of areal capacitance with a value of 5.3 mF cm^{-2} for 10 µm thick paper electrode (Table S1, Supporting Information).[19,41,47] Additionally, all spray-coated paper µSCs achieve comparable values among µSCs based on solution processing[43,48,49] (printed), electropolymerized conductive polymers,[26,50,51] and other deposition methods.[52–54]

In order to demonstrate the maximum energy and power density of the P-µSC, a Ragone Plot is given in Figure 2f. Considering the total volume of the devices, the P-µSC (total thickness $\approx$11 µm) delivered a volumetric energy density of 0.26 mWh cm^{-3} and a power density of 270 mW cm^{-3}. The device places well in between the Li-thin film battery[52] and Al electrolytic capacitor[55] by exhibiting two orders of magnitude higher power density than Li-thin film battery and three orders of magnitude higher energy density than the electrolytic capacitor.

To give a complete insight of the performance, full electrochemical characterization of the 11 µm P-µSC is given in **Figure 3**. Figure 3a,b demonstrates the CV curves of the device at different scan rates within a voltage range from 0 to 0.8 V. Between scan rate 1 to 100 mV s^{-1}, the device shows rectangular, symmetric CV curves, indicating good capacitive performance with high-rate capability. Figure 3c displays the GCD curves at increasing current densities from 0.0125 to 0.2 mA cm^{-2}, showing identical triangular shapes and exhibiting the highest coulombic efficiency of 97.4%. Additionally, our device shows a good coulombic efficiency with different current densities, indicating wide range rate capability performance (Figure S4, Supporting Information). It should be noted that even for the planar structure (w = 1.0 mm) and high currents (0.1 mA cm^{-2}), the device loses its 9% charge on the onset of discharge with 70 mV IR drop. The highest areal and volumetric capacitance achieved is 3.18 mF cm^{-2} and 7.0 F cm^{-3} at a current density of 0.0125 mA cm^{-2} (Figure 3d). To investigate the ESR and charge transfer mechanism, impedance spectroscopy is conducted between 100 kHz and 10 mHz, as shown in Figure 3e. The absence of a semicircle in the high-frequency region shows low charge transfer resistance, and a steeper line at low-frequency region indicates good ion diffusion[27] (Nyquist plot, Figure 3e, inset). Additionally, we have demonstrated electrochemical stability of a device with 4.5 µm electrode thickness by showing the impedance spectrum after 10 000 GDC cycles at 0.1 mA cm^{-2} (Figure 3e) as well as 1000 EIS cycles, which show minimal change (Figure S5, Supporting Information). All spray-coated paper µSCs with an overall package thickness of $\approx$11 µm show stable cycle performance as shown in Figure 3f, with capacitance retention of 90% after 10 000 cycles. This long-term operation capability is even higher than inorganic competitors such as NiO (10 000 cycles, 81%)[46], carbon nanotubes (10 000 cycles, 88%),[47] and MoS$_2$[56] (10 000 cycles, 85.6%), and graphene/NiOOH/NiO$_2$ (3000 cycles, 80%)[57], indicating that solution-processed paper electrodes have superior long-term operation capability. Additionally, the device exhibits an areal energy density of 0.283 µWh cm^{-2} and a power density of 0.65 mW cm^{-2} (volumetric energy density of 0.26 mWh cm^{-3} and power density of 270 mW cm^{-3}), when the total device area and volume are considered (Figure S6, Supporting Information). These values are better or comparable for the classes of both PEDOT and other active material based µSCs.[41,43,49,56,58,59]

Devices for skin electronics need precise control of spatial device dimensions while maintaining minimal component area and volume. Inactive volume/mass of device components (bulky substrates and packaging material) in battery systems can occupy up to 70% of the overall volume and limit design concepts in e-skin and implantable devices.[60,61] [62] One successful attempt was performed with a unique cell design with
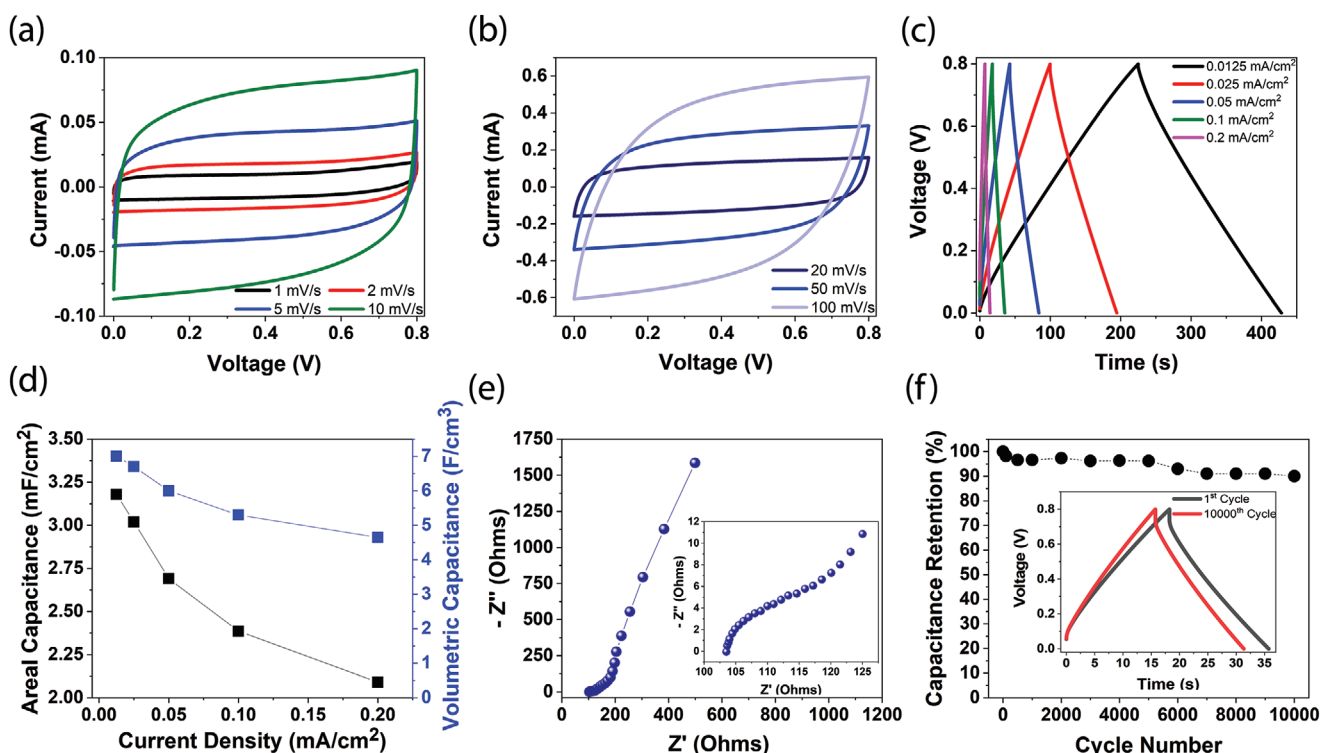
Figure 3. Electrochemical characterization of micro-supercapacitors with 4.5 µm thick electrode. a) Low scan rate CV (1–10 mV s^{-1}), b) CV with high scan rate (20–100 mV s^{-1}), c) GCD at different current densities. d) Calculated areal and volumetric capacitance at different current densities, extracted from GCD curves in c). e) Nyquist plot of ≈11 µm thick µSC, inset zoomed in high frequency region. f) Charge–discharge cycling performance, inset shows the first and 10 000th GCD curve of the device at 0.1 mA cm^{-2}.

45% of electrode volume with an optimal footprint.[63] However, alternative routes in achieving perfectly designed energy storage devices are lacking.[64] Ultrathin substrates and packaging with planar electrodes would suffice well-packed architectures. Minimizing bulky components and reduction of overall mass in the cell design leads to higher energy and power densities and eventually enhancing the position in the Ragone plot.[64] To achieve the goals mentioned above, ultrathin substrates with ultrathin packaging materials can be used for e-skin compatible energy storage devices. The Ragone plot is given to compare the performance of P-µSC with previous paper-based supercapacitors when the total device mass is considered (Figure S7, Supporting Information). It should be noted that the packaging material for the P-µSC consists of 1 µm thick parylene C. With complete control of each layer thickness and configuration, the electrode occupies 40% of the thickness and the overall active layer mass is ≈66% (electrode and electrolyte).

To investigate mechanical stability and obtain information about mechanical properties of ultrathin systems, we have performed finite element analysis (FEA) of stress and strain distributions at a bending radius 6 mm of the µSC. The finite element method (FEM) for FEA has proven to be a powerful tool in analyzing the mechanical properties of various flexible devices.[36,65–68] To get a deeper understanding of strain and stress values on the supercapacitor during a radial deformation, we have performed numerical simulations of representative parts of the µSC (**Figure** 4a) using a COMSOL software package.[69]

In the case of radial deformation in layered structures, strains can be described by the concept of a neutral plane. The material remains unstrained within this plane and is stretched above or compressed below the mechanical neutral plane (Figure S8a, Supporting Information). The position of the neutral plane is calculated according to the formula[36,70]

$$b = \frac{\sum_{i=1}^{n} \tilde{E}_i d_i \left[\left(\sum_{j=1}^{i} d_j \right) - d_i/2 \right]}{\sum_{i=1}^{n} \tilde{E}_i d_i} \tag{1}$$

$$\tilde{E}_i = E_i \left(1 - v_i^2\right) \tag{2}$$

where E_i—Young's modulus, v_i—Poisson coefficient, d_i—thickness, and i corresponds to each of the layers. Assuming a parylene C layer thickness of 2.8 µm, the paper electrode 4 µm, and the gel electrolyte 4 µm, the neutral plane is located inside the parylene C domain at a distance of 0.76 nm from its center (Figure S8b, Supporting Information). This means that due to the large Young's modulus of parylene C (2.8 GPa) compared to the paper electrode (400 kPa) or gel electrolyte (32 kPa), the bottom half of parylene C domain will compress and the top half of parylene will stretch in reaction to the radial deformation with the paper electrode and gel electrolyte (Figure 4b).

As a simple approximation, the value of strain in the material at a distance b, from the neutral plane, created by a radial deformation, can be estimated with the formula[36,71]

$$\varepsilon = b/R \tag{3}$$

**ADVANCED
SCIENCE NEWS**

www.advancedsciencenews.com

**ADVANCED
MATERIALS
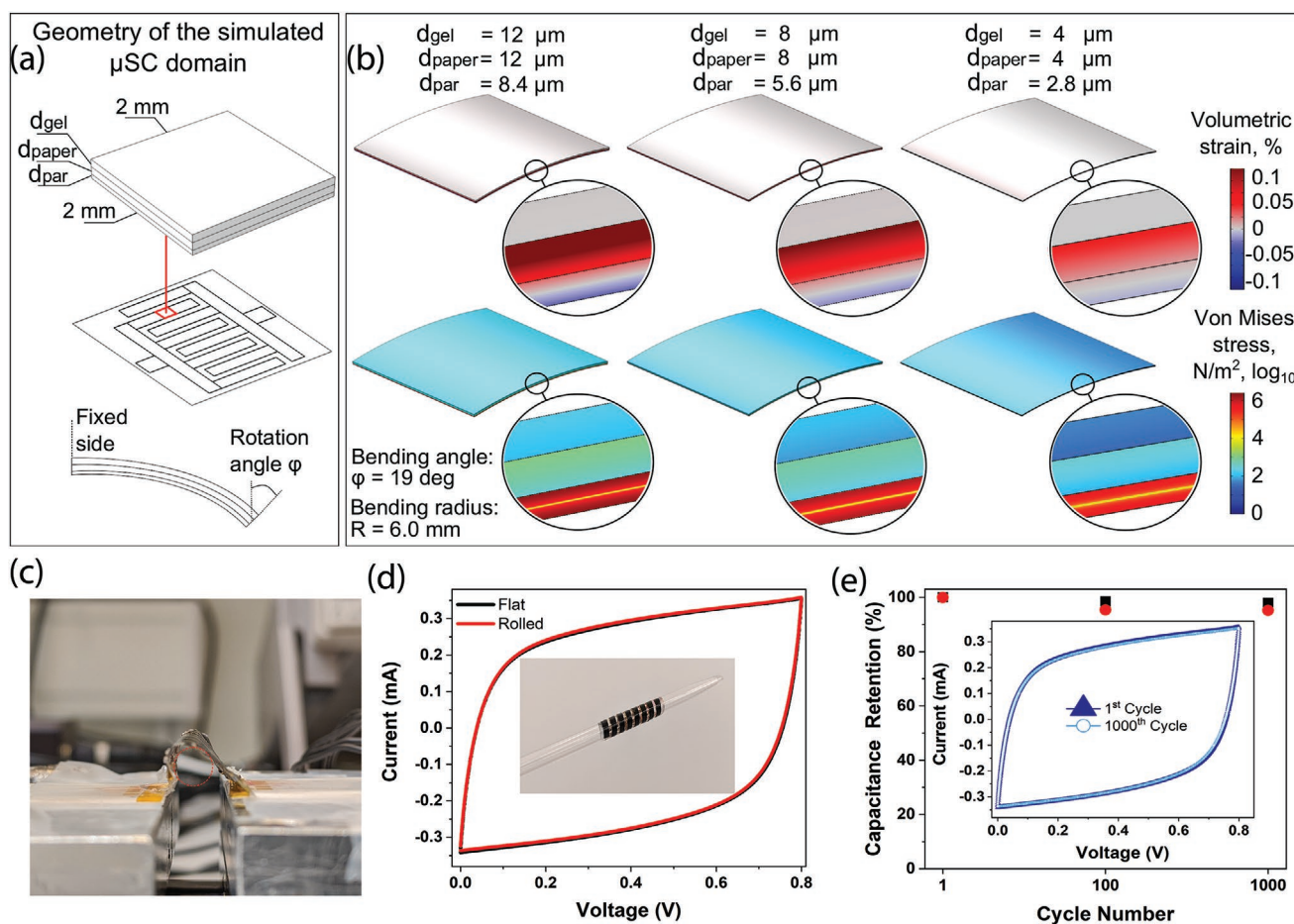TECHNOLOGIES**

www.advmattechnol.de

Figure 4. Mechanical performance of P-μSCs. a) Geometry of the simulated model of microsupercapacitor. b) Simulated volumetric strain and von Mises stress surfaces of the electrode area (2 × 2 mm²) at different layer thicknesses and radial deformation 6 mm. c) Picture of the μSC at a bending radius of ≈6 mm. d) CV of an ≈11 μm thick device at 50 mV s⁻¹ when it is flat or rolled, inset shows the picture of the device is rolled on a glass rod of 5 mm diameter. e) Capacitance retention after 1000 bending cycles, inset shows the first and 1000th CV at 50 mV s⁻¹.

where R is the radius of deformation. Assuming $R = 6$ mm, the predicted ε value at 10 μm from the neutral plane is ± 0.166%, which means that overall strain in the device is minor and none of the domains will overcome the linear deformation regime. Experimentally observed radial deformation is reproduced with one side of a device fixed, and the opposite side subjected to the prescribed rotation (Figure S13a, Supporting Information).

The strain and stress distribution in the layered structures with the exact thickness of all domains as in the fabricated devices are shown in Figure 4b ($d_{paper} = 4$ μm, $d_{gel} = 4$ μm, $d_{par} = 2.8$ μm). The parylene C substrate is subjected to stretching/compression approximately in a range from −0.007% to +0.007% at the maximum bending radius of 6 mm. The paper electrode domains are located on top of the mechanical neutral plane and are subjected to stretching with increased values toward the top of the layer. The resulting volumetric strain is in the range of 0.012–0.045%. For the gel electrolyte domain, the volumetric strain is negligibly low due to the Poisson coefficient of 0.499, meaning that the gel electrolyte was modeled as an almost incompressible material. The calculated von Mises stress surfaces for different displacement values are plotted in

Figure 4b. The stress accumulates proportionally to Young's modulus with the highest values throughout the parylene C substrate and lowest for the gel electrolyte domain.

With an increase of each domain thickness, both volumetric strain and von Mises stress grow proportionally. For instance, the volumetric strain in a parylene C layer with $d_{par} = 12$ μm is in the range between −0.024% and +0.024%. For the paper electrode domain with $d_{paper} = 12$ μm, volumetric strain reaches a reasonably high value of 0.15%, which may cause irreversible changes in the paper structure (Figure 4b). From the point of mechanical stability for the case of radial deformations, the paper electrode is the most prominent. Ensuring the electrode's thickness for values approximately less than 10 μm leads to sustainable repeated deformations at $R = 6$ mm.

It should be noted that the device geometry is more complicated than the layered structure. The flexible μSC was also simulated in the form of the layered "four-finger" geometry, fully mimicking the experimental geometry but with the increased thickness of each layer and smaller radial deformations to achieve convergence of the simulation (Figure S15, Supporting Information). The distance between the "finger electrode" gives a space for the electrode and the gel electrode to deform in order

**ADVANCED
SCIENCE NEWS**
www.advancedsciencenews.com

**ADVANCED
MATERIALS
TECHNOLOGIES**
www.advmattechnol.de

to compensate stress created by radial deformations. However, the "finger" geometry of the electrode layer does not significantly affect the mechanical properties of the layered structure. The reason behind is that parylene C substrate remains as the most rigid part of the device, while the paper electrode and gel electrolyte follow the deformed shape of the parylene C.

As a brief conclusion, the simulations showed that the µSC, subjected to radial deformations is mechanically stable within the mechanical neutral plane, located inside parylene C layer. Due to the large Young's modulus, the shape of parylene C substrate defines the strain directions for other µSC layers, such as paper electrode and gel electrolyte. The largest volumetric strain is observed in electrode domain (Figure 4b) with maximal values of 0.045% at bending radius $R = 6$ mm. Assuming the bending radius 6 mm, the device will remain stable after deformation under condition that the electrode thickness is less than 10 µm.

Since the simulation results show low stress and strain values, we aimed to investigate electrochemical stability under bending conditions. Figure 4b shows the image of the P-µSC in the bending state; a red circle indicates a bending radius of 6 mm (the same value was used during the simulations). Additional CV tests were carried out to evaluate the performance of the device under various deformations. Figure 4c shows the CV curves at a scan rate of 50 mV s^{-1} when the device is flat and rolled (the inset of Figure 4c shows a µSC rolled onto a glass rod of a diameter of 5 mm, which shows operation bending radius of 2.5 mm, Figure S9, Supporting Information). In addition, the µSC exhibits identical CV curves and negligible changes after 1000 deformation cycles, retaining 98% of initial capacitance (Figure 4d and inset, Supporting Information), thus demonstrating excellent stability under mechanical load (Table S2, Supporting Information).

To boost the operation voltage and increase the capacitance of the on-chip device, multiple P-µSCs can be easily connected in series. **Figure 5**a shows the CV of an individual device and two/three connected in series at a scan rate of 20 mV s^{-1}

(GCD current density of 0.05 mA cm^{-2} can be found in Figure S10, Supporting Information). With this configuration, it is shown that the stack voltage can reach 2.4 V, which is quite sufficient for low-power sensors and displays. To demonstrate an on-chip and wearable system, we have printed an electrochromic (EC) display onto an ultrathin substrate. Next, two flexible µSCs were connected in series to operate the EC display (Figure 5b). Details regarding the electrochromic display can be found in the Experimental Section. To demonstrate the skin-mountable, wearable P-µSC/EC display system (Figure S11, Supporting Information), the two µP-SCs in series are charged up to 2.0 V and EC display is operated by a charged supercapacitor module. The proof-of-concept demonstration shows the possibility to integrate different technologies and develop applications designed for e-skin and wearable electronics.

3. Conclusion

In summary, we have demonstrated a versatile route to fabricate skin-compatible, ultrathin microsupercapacitors using sequential spray coating. Both cellulose-based electrode and electrolyte were deposited by airbrush-assisted spray coating on ultrathin 2.8 µm parylene C substrates. Excellent control over the layer thickness leads to a device with a total thickness of 10.5 ± 0.3 µm. The developed architecture of the energy storage device allowed us to minimize the mass and volume of the inactive components and increase the volume fraction of the active layer up to 40%, enhancing the position in the Ragone plot. Fabricated P-µSCs proved to be mechanically stable under various deformations and maintain 98% of capacitance after 1000 bending cycles. The P-µSCs were interfaced to power up a printed electrochromic display as an example of possible on-chip application. The developed concept of ultrathin energy storage devices with cellulose-based electrodes is promising for both supplying power and biomedical sensory systems,
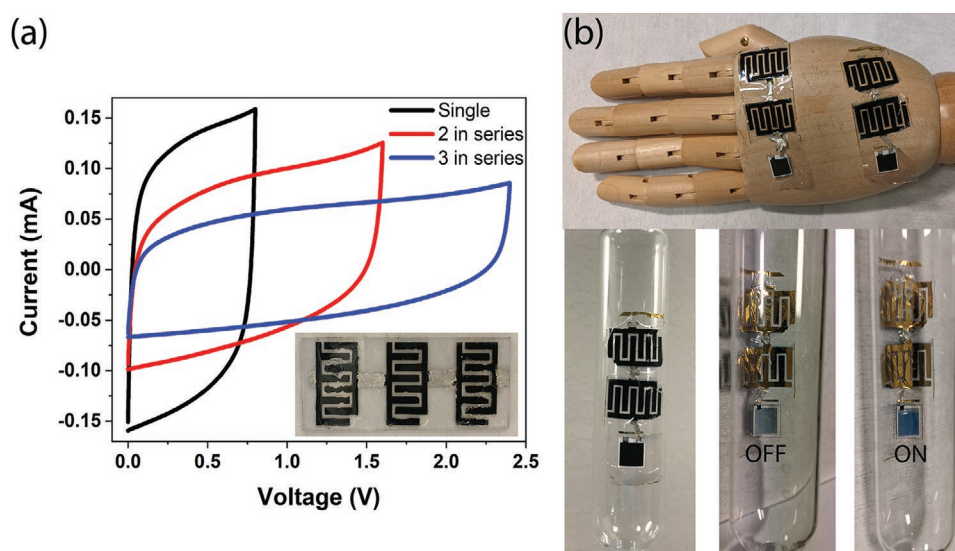

Figure 5. Applications of spray coated paper micro-supercapacitors. a) CV of series connected micro-supercapacitors, inset: optical image of three P-µSCs in series. b) Pictures of µSC/EC display systems, laminated onto curved glass tubes, to highlight the visibility.

motivating the advancement toward all cellulose, scalable, sustainable, and low-cost devices.

4. Experimental Section

Reagent and Materials: Poly(3,4-ethylenedioxythiophene):poly(styrene sulfonate) (PEDOT:PSS) Clevios PH1000 was purchased from Heraeus Clevios GmbH. Ethylene Glycol, Glycerol, Hydroxyethyl cellulose (HEC, M_w = 250 000), 1-ethyl-3- methylimidazolium ethyl sulfate (EMIM-ES, >95%) were purchased from Sigma-Aldrich. 0.52 wt% CNF dispersed in water was purchased from RISE Bioeconomy. The distilled water (DI) was used as solvent for all the inks.

Ink Preparation: Paper electrode ink was prepared by mixing CNF, PEDOT: PSS, and additives at room temperature[29]. Briefly, PEDOT: PSS was filtered through a 0.45 µm PVDF filter, CNF dispersion was diluted down to 0.1 wt% with deionized water (DI). The ratio between the PEDOT: PSS/CNF/EG/Glycerol is kept the same as Say et al.[29] The ink was homogenized by Ultra-Turrax for 5 min. Data on the viscosity of the ink, is available in Figure S12 (Supporting Information). Gel electrolyte was prepared by mixing EMIM:ES and DI water in a ratio of 1:12, then 6 wt% HEC was added. The mixture was vigorously stirred at 90 °C for ≈1 h until it becomes a homogeneous solution and degassed for 15 min.

Fabrication of Microsupercapacitors: A 2.8 µm thick parylene C layer was deposited on glass substrates using a Diener Electronic GmbH CVD system. A 5 nm Cr (adhesion layer) and 95 nm Au (current collector) were thermally evaporated through a shadow mask. Substrates were placed on a hot plate at 90 °C for 15 min prior to spraying the electrode and electrolyte. The paper electrode ink was spray-coated with an airbrush (CoCraft, 35 mm nozzle) using 3.0 bar on patterned current collectors through a stainless-steel shadow mask (thickness of 75 µm). The airbrush was placed 12 cm above the substrate, and spraying protocol was followed (1 s of spraying, 10 s of waiting). Finally, the gel electrolyte was spray coated on the electrode. The airbrush was placed 7 cm above the substrate and spraying protocol was followed (2 s of spraying, 20 s of waiting). For the series connection of the devices, silver paste (Ferro GmbH) was stencil printed to connect the microsupercapacitors after the fabrication of µSCs. An informed signed consent was obtained from the human subject of the experiments for the skin compatible device demonstration.

Mechanical Modeling: Simulations of the stress and strain distributions inside the device were conducted with finite element analysis (FEA) implemented in COMSOL 5.5 software package (https://www.comsol.com/product-download).

Coordinates of the simulated system were defined with the following equation[72]

$$x = X + u(X,t) \tag{4}$$

where X are material coordinates and u—displacement field.

The governing equations of the model are[72]

$$\nabla \cdot (FS)^T + f_v = 0 \tag{5}$$

$$F = \frac{\partial x}{\partial X} = I + \nabla u \tag{6}$$

where F is a total deformation gradient tensor, S—second Piola–Kirchhoff stress tensor, f_v—volumetric forces (force per deformed volume), and I—identity tensor.

Deformation of the device geometry was implemented in a way to mimic the experimental studies: left side was fixed, and the right side was shifted to the left (Note S1 and Figures S13–S15, Supporting Information). Corresponded boundary conditions are represented with constraints on displacements for parylene C layer sides (Figure S13, Supporting Information).

Fixed constrained at the left side forbids all movement of the left boundary[72]

$$u_x = u_y = u_z = 0 \tag{7}$$

Prescribed rotation at the right side (around the axis, located in the geometrical center of the face as shown in Figure 4a) creates radial deformation and is implemented with the "rigid connector" boundary condition[72]

$$\varphi = 1[\text{deg}] * P \tag{8}$$

Parameter P was in range from 0 to 19 for a finger part and from 0 to 60 for a full device with a step of 0.1. Stationary solution for every P was used as initial values for the simulation for the next P. This procedure allowed us to obtain smooth deformation of the simulated device close to the experimental conditions.

Von Mises stress was calculated with formula[72]

$$\sigma_{\text{mises}} = \sqrt{\frac{1}{2}\left((\sigma_{11} - \sigma_{22})^2 + (\sigma_{22} - \sigma_{33})^2 + (\sigma_{33} - \sigma_{11})^2 + \sigma_{12}^2 + \sigma_{23}^2 + \sigma_{31}^2\right)} \tag{9}$$

where σ_{11}, σ_{22}, σ_{33}, σ_{12}, σ_{23}, σ_{31} are Cauchy stress tensor components.

Volumetric strain was calculated as [72]

$$\varepsilon_{\text{vol}} = trace(\varepsilon) \tag{10}$$

where ε is strain tensor.

Application: Fabrication Details for Electrochromic Displays (ECDs): Electrolyte ink for the display application, was made in-house by RISE Printed electronics. Commercially available, Poly(3,4-ethylenedioxythiophene) polystyrene sulfonate ink, (PEDOT: PSS, (Clevios S V4, Heraeus) a dielectric ink (5018, Dupont), and carbon ink (7102, Dupont) were used as received.

Manufacture of all printed electrochromic displays was performed by the following steps:

Two layers of commercially available PEDOT: PSS ink were printed on the parylene C substrate, and each layer cured by heat at 80 °C in a square display design. Next, two layers of the dielectric ink were deposited, and each layer was cured by UV to define the active switching area. Two layers of the RISE standard electrolyte was printed into the opening of the dielectric, and each was cured by UV. The two carbon layers were printed lastly and cured by heat at 80 °C, which act as the counter electrode in all screen-printed electrochromic display.

The all-printed electrochromic displays were electrochemically characterized using a potentiostat (Octastat, Ivium) and handheld spectrophotometer for their cyclic voltammetry and their switching behavior. The cyclic voltammetry was before in the range of 3 to −3 V at a scan rate of 100 mV s^{-1} and the switching using a pulse wave from 3 to −1 V for 5 s (Note S2 and Figure S16, Supporting Information). The color contrast was calculated from the measurements of the handheld spectrophotometer and details are given in Table S4, Supporting Information).

Characterization: Thickness measurements were performed by Dektak, digital micrometer (Mitutoyo) and confirmed with SEM (Gemini 300, Zeiss). Two electrode electrochemical measurements (Cyclic Voltammetry (CV) galvanostatic charge/discharge measurements (GCD) and Impedance Spectroscopy) were performed with Biologic SP-200 potentiostat. CV was carried out from 1 to 100 mV s^{-1}, constant current method GCD measurements were carried out between 10 µA cm^{-2} and 0.2 mA cm^{-2}.

The capacitance was calculated from the discharge curves of the galvanostatic measurements using Equation (11), respectively,

$$\text{Capacitance } (C) = \frac{\Delta t \times I}{V} \tag{11}$$

Where Δt is the discharge time, I is the discharge current, V is the voltage. Energy density and power density were calculated using Equation (12), Equation (13), and respectively

$$\text{Energy Density} = E = \frac{1}{2A}CV^2 \tag{12}$$

$$\text{Power Density} = P = \frac{E}{\Delta t V} \tag{13}$$

$$P_{\text{max}} = \frac{V^2}{4AR} \tag{14}$$

C is the capacitance; V is the operating voltage. For areal and volumetric energy and power densities, electrode area A (cm^2), volume (cm^3), and R (ESR) is used, respectively.

Supporting Information

Supporting Information is available from the Wiley Online Library or from the author.

Conflict of Interest

The authors declare no conflict of interest.

Data Availability Statement

The data that support the findings of this study are available from the corresponding author upon reasonable request.

[1] C. García Núñez, L. Manjakkal, R. Dahiya, *npj Flex. Electron.* **2019**, *3*, 1.
[2] D. P. Dubal, N. R. Chodankar, D. H. Kim, P. Gomez-Romero, *Chem. Soc. Rev.* **2018**, *47*, 2065.
[3] S. Gong, W. Cheng, *Adv. Energy Mater.* **2017**, *7*, 1700648.
[4] L. Lu, Z. Yang, K. Meacham, C. Cvetkovic, E. A. Corbin, A. Vázquez-Guardado, M. Xue, L. Yin, J. Boroumand, G. Pakeltis, T. Sang, K. J. Yu, D. Chanda, R. Bashir, R. W. Gereau, X. Sheng, J. A. Rogers, *Adv. Energy Mater.* **2018**, *8*, 1703035.
[5] K. Fukuda, K. Yu, T. Someya, *Adv. Energy Mater.* **2020**, *10*, 2000765.
[6] Y. R. Jeong, G. Lee, H. Park, J. S. Ha, *Acc. Chem. Res.* **2019**, *52*, 91.
[7] R. Liu, M. Takakuwa, A. Li, D. Inoue, D. Hashizume, K. Yu, S. Umezu, K. Fukuda, T. Someya, *Adv. Energy Mater.* **2020**, *10*, 2000523.
[8] A. M. Zamarayeva, A. E. Ostfeld, M. Wang, J. K. Duey, I. Deckman, B. P. Lechêne, G. Davies, D. A. Steingart, A. C. Arias, *Sci. Adv.* **2017**, *3*, e1602051.
[9] J. Dodd, C. Kishiyama, H. Mukainakano, M. Nagata, H. Tsukamoto, *J. Power Sources* **2005**, *146*, 784.
[10] A. T. Kutbee, R. R. Bahabry, K. O. Alamoudi, M. T. Ghoneim, M. D. Cordero, A. S. Almuslem, A. Gumus, E. M. Diallo, J. M. Nassar, A. M. Hussain, N. M. Khashab, M. M. Hussain, *npj Flex. Electron.* **2017**, *1*, 7.
[11] M. Koo, K. Il Park, S. H. Lee, M. Suh, D. Y. Jeon, J. W. Choi, K. Kang, K. J. Lee, *Nano Lett.* **2012**, *12*, 4810.
[12] C. Zhao, Y. Liu, S. Beirne, J. Razal, J. Chen, *Adv. Mater. Technol.* **2018**, *3*, 1800028.
[13] Y. Z. Zhang, Y. Wang, T. Cheng, L. Q. Yao, X. Li, W. Y. Lai, W. Huang, *Chem. Soc. Rev.* **2019**, *48*, 3229.
[14] F. Bu, W. Zhou, Y. Xu, Y. Du, C. Guan, W. Huang, *npj Flex. Electron.* **2020**, *4*, 31.
[15] D. Li, S. Yang, X. Chen, W. Y. Lai, W. Huang, *Adv. Funct. Mater.* **2021**, *31*, 2107484.
[16] T. Cheng, Y. W. Wu, Y. L. Chen, Y. Z. Zhang, W. Y. Lai, W. Huang, *Small* **2019**, *15*, 1901830.
[17] J. Pu, X. Wang, R. Xu, S. Xu, K. Komvopoulos, *MicrosystemsNanoeng.* **2018**, *4*, 16.
[18] Y. Yun, K. R. Nandanapalli, J. H. Choi, W. Son, C. Choi, S. Lee, *Nano Energy* **2020**, *78*, 105356.
[19] Z. Liu, Z. S. Wu, S. Yang, R. Dong, X. Feng, K. Müllen, *Adv. Mater.* **2016**, *28*, 2217.
[20] H. Wang, Y. Diao, Y. Lu, H. Yang, Q. Zhou, K. Chrulski, J. M. D'Arcy, *Nat. Commun.* **2020**, *11*, 3882.
[21] Y. Diao, Y. Lu, H. Yang, H. Wang, H. Chen, J. M. D'Arcy, *Adv. Funct. Mater.* **2020**, *30*, 2003394.
[22] G. S. Gund, J. H. Park, R. Harpalsinh, M. Kota, J. H. Shin, T. il Kim, Y. Gogotsi, H. S. Park, *Joule* **2019**, *3*, 164.
[23] Y. Liu, B. Weng, Q. Xu, Y. Hou, C. Zhao, S. Beirne, K. Shu, R. Jalili, G. G. Wallace, J. M. Razal, J. Chen, *Adv. Mater. Technol.* **2016**, *1*, 1600166.
[24] T. Wakabayashi, M. Katsunuma, K. Kudo, H. Okuzaki, *ACS Appl. Energy Mater.* **2018**, *1*, 2157.
[25] A. Elschner, S. Kirchmeyer, W. Lovenich, U. Merker, K. Reuter, *PEDOT: Principles and Application of an Intrinsically Conducting Polymer*, CRC Press, Boca Raton, FL, USA **2010**.
[26] N. Kurra, M. K. Hota, H. N. Alshareef, *Nano Energy* **2015**, *13*, 500.
[27] Q. Jiang, N. Kurra, H. N. Alshareef, *Adv. Funct. Mater.* **2015**, *25*, 4976.
[28] J. Li, W. Yan, G. Zhang, R. Sun, D. Ho, *J. Mater. Chem. C* **2021**, *9*, 1685.
[29] M. G. Say, R. Brooke, J. Edberg, A. Grimoldi, D. Belaineh, I. Engquist, M. Berggren, *npj Flex. Electron.* **2020**, *4*, 14.
[30] Y. Wen, J. Xu, *J. Polym. Sci. Part A: Polym. Chem.* **2017**, *55*, 1121.
[31] C. Girotto, D. Moia, B. P. Rand, P. Heremans, *Adv. Funct. Mater.* **2011**, *21*, 64.
[32] A. Baldelli, A. Amirfazli, J. Ou, W. Li, *Langmuir* **2020**, *36*, 11393.
[33] N. Singh, C. Galande, A. Miranda, A. Mathkar, W. Gao, A. Leela, M. Reddy, A. Vlad, P. M. Ajayan, *Sci. Rep.* **2012**, *2*, 481.
[34] Z. S. Wu, Z. Liu, K. Parvez, X. Feng, K. Müllen, *Adv. Mater.* **2015**, *27*, 3669.
[35] Z. Wang, Y. H. Lee, S. W. Kim, J. Y. Seo, S. Y. Lee, L. Nyholm, *Adv. Mater.* **2021**, *33*, 2000892.
[36] L. Mao, Q. Meng, A. Ahmad, Z. Wei, *Adv. Energy Mater.* **2017**, *7*, 1700535.
[37] D. Qi, Y. Liu, Z. Liu, L. Zhang, X. Chen, *Adv. Mater.* **2017**, *29*, 1602802.
[38] A. Vahidmohammadi, J. Moncada, H. Chen, E. Kayali, J. Orangi, C. A. Carrero, M. Beidaghi, *J. Mater. Chem. A* **2018**, *6*, 22123.
[39] Y. Xu, Y. Tao, X. Zheng, H. Ma, J. Luo, F. Kang, Q. H. Yang, *Adv. Mater.* **2015**, *27*, 8082.
[40] I. Sahalianov, M. G. Say, O. S. Abdullaeva, F. Ahmed, E. Glowacki, I. Engquist, M. Berggren, I. Zozoulenko, *ACS Appl. Energy Mater.* **2021**, *4*, 8629.
[41] M. Yoonessi, A. Borenstein, M. F. El-Kady, C. L. Turner, H. Wang, A. Z. Stieg, L. Pilon, *ACS Appl. Energy Mater.* **2019**, *2*, 4629.

[42] Y. Wu, Y. Zhang, Y. Liu, P. Cui, S. Chen, Z. Zhang, J. Fu, E. Xie, *ACS Appl. Mater. Interfaces* **2020**, *12*, 42933.

[43] J. Li, S. Sollami Delekta, P. Zhang, S. Yang, M. R. Lohe, X. Zhuang, X. Feng, M. Östling, *ACS Nano* **2017**, *11*, 8249.

[44] D. Kim, G. Lee, D. Kim, J. S. Ha, *ACS Appl. Mater. Interfaces* **2015**, *7*, 4608.

[45] P. Zhang, J. Wang, W. Sheng, F. Wang, J. Zhang, F. Zhu, X. Zhuang, R. Jordan, O. G. Schmidt, X. Feng, *Energy Environ. Sci.* **2018**, *11*, 1717.

[46] S. Qin, Q. Zhang, X. Yang, M. Liu, Q. Sun, Z. L. Wang, *Adv. Energy Mater.* **2018**, *8*, 1800069.

[47] H. Kim, J. Yoon, G. Lee, S. H. Paik, G. Choi, D. Kim, B. M. Kim, G. Zi, J. S. Ha, *ACS Appl. Mater. Interfaces* **2016**, *8*, 16016.

[48] B. D. Boruah, A. Maji, A. Misra, *ACS Appl. Mater. Interfaces* **2018**, *10*, 15864.

[49] A. Valero, A. Mery, D. Gaboriau, P. Gentile, S. Sadki, *ACS Appl. Energy Mater.* **2019**, *2*, 436.

[50] B. Song, L. Li, Z. Lin, Z. K. Wu, K. sik Moon, C. P. Wong, *Nano Energy* **2015**, *16*, 470.

[51] S. Liu, J. Xie, H. Li, Y. Wang, H. Y. Yang, T. Zhu, S. Zhang, G. Cao, X. Zhao, *J. Mater. Chem. A* **2014**, *2*, 18125.

[52] D. Pech, M. Brunet, H. Durou, P. Huang, V. Mochalin, Y. Gogotsi, P. L. Taberna, P. Simon, *Nat. Nanotechnol.* **2010**, *5*, 651.

[53] Y. Wang, L. Sun, P. Song, C. Zhao, S. Kuang, H. Liu, D. Xiao, F. Hu, L. Tu, *J. Power Sources* **2020**, *448*, 227415.

[54] J. Lin, C. Zhang, Z. Yan, Y. Zhu, Z. Peng, R. H. Hauge, D. Natelson, J. M. Tour, *Nano Lett.* **2013**, *13*, 72.

[55] S. De Liberato, C. Ciuti, D. Auston, M. Nuss, S. Keiding, M. Van Exter, C. Fattinger, A. J. Taylor, C. Highstrete, M. Lee, R. D. Averitt, E. Smirnova, A. Azad, H. Chen, G. Scalari, M. I. Amanti, M. Beck, J. Faist, *Science* **2012**, *335*, 1326.

[56] B. Li, X. Liang, G. Li, F. Shao, T. Xia, S. Xu, N. Hu, Y. Su, Z. Yang, Y. Zhang, *ACS Appl. Mater. Interfaces* **2020**, *12*, 39444.

[57] X. Feng, J. Ning, D. Wang, J. Zhang, J. Dong, C. Zhang, X. Shen, Y. Hao, *J. Power Sources* **2019**, *418*, 130.

[58] S. W. Kim, K. N. Kang, J. W. Min, J. H. Jang, *Nano Energy* **2018**, *50*, 410.

[59] G. Lee, J. W. Kim, H. Park, J. Y. Lee, H. Lee, C. Song, S. W. Jin, K. Keum, C. H. Lee, J. S. Ha, *ACS Nano* **2019**, *13*, 855.

[60] X. Yue, J. Grzyb, A. Padmanabha, J. H. Pikul, *Energies* **2020**, *13*, 2492.

[61] L. Liu, Q. Weng, X. Lu, X. Sun, L. Zhang, O. G. Schmidt, *Small* **2017**, *13*, 1701847.

[62] X. Huang, L. Wang, H. Wang, B. Zhang, X. Wang, R. Y. Z. Stening, X. Sheng, L. Yin, *Small* **2020**, *16*, 1902827.

[63] W. Lai, C. K. Erdonmez, T. F. Marinis, C. K. Bjune, N. J. Dudney, F. Xu, R. Wartena, Y. M. Chiang, *Adv. Mater.* **2010**, *22*, E139.

[64] J. Betz, G. Bieker, P. Meister, T. Placke, M. Winter, R. Schmuch, *Adv. Energy Mater.* **2019**, *9*, 1900761.

[65] G. Kettlgruber, D. Danninger, R. Moser, M. Drack, C. M. Siket, D. Wirthl, F. Hartmann, G. Mao, M. Kaltenbrunner, S. Bauer, *Adv. Intell. Syst.* **2020**, *2*, 2000065.

[66] J. T. B. Overvelde, Y. Mengüç, P. Polygerinos, Y. Wang, Z. Wang, C. J. Walsh, R. J. Wood, K. Bertoldi, *Extrem. Mech. Lett.* **2014**, *1*, 42.

[67] I. Chang, T. Park, J. Lee, M. H. Lee, S. H. Ko, S. W. Cha, *J. Mater. Chem. A* **2013**, *1*, 8541.

[68] B. Ji, Z. Xie, W. Hong, C. Jiang, Z. Guo, L. Wang, X. Wang, B. Yang, J. Liu, *J. Mater.* **2020**, *6*, 330.

[69] COMSOL Multiphysics® v. 5.5. COMSOL AB, *Stock. Sweden* (accessed: June 2021).

[70] S. Il Park, A. P. Le, J. Wu, Y. Huang, X. Li, J. A. Rogers, *Adv. Mater.* **2010**, *22*, 3062.

[71] Z. Suo, E. Y. Ma, H. Gleskova, S. Wagner, *Appl. Phys. Lett.* **1999**, *74*, 1177.

[72] "Structural Mechanics Module Users Guide," https://doc.comsol.com/5.4/doc/com.comsol.help.sme/StructuralMechanicsModuleUsersGuide.pdf (accessed: June 2021).